

HSIM: a simulation pipeline for the HARMONI integral field spectrograph on the European ELT

S. Zieleniewski^{1*} N. Thatte¹ S. Kendrew¹ R. C. W. Houghton¹
A. M. Swinbank² M. Tecza¹ F. Clarke¹ T. Fusco^{3,4}

¹*Astrophysics, Denys Wilkinson Building, Keble Road, Oxford, OX1 4RH*

²*Institute for Computational Cosmology, University of Durham, South Road, Durham, DH1 4LH*

³*ONERA, BP 72, F-92322, Chatillon, France*

⁴*Aix Marseille University, CNRS LAM (Laboratoire d'Astrophysique de Marseille) UMR 7326, 13388 Marseille, France*

Last updated 18/08/15

ABSTRACT

We present HSIM: a dedicated pipeline for simulating observations with the HARMONI integral field spectrograph on the European Extremely Large Telescope. HSIM takes high spectral and spatial resolution input data-cubes, encoding physical descriptions of astrophysical sources, and generates mock observed data-cubes. The simulations incorporate detailed models of the sky, telescope and instrument to produce realistic mock data. Further, we employ a new method of incorporating the strongly wavelength dependent adaptive optics point spread functions. HSIM provides a step beyond traditional exposure time calculators and allows us to both predict the feasibility of a given observing programme with HARMONI, as well as perform instrument design trade-offs. In this paper we concentrate on quantitative measures of the feasibility of planned observations. We give a detailed description of HSIM and present two studies: estimates of point source sensitivities along with simulations of star-forming emission-line galaxies at $z \sim 2-3$. We show that HARMONI will provide exquisite resolved spectroscopy of these objects on sub-kpc scales, probing and deriving properties of individual star forming regions.

Key words: instrumentation: spectrographs - instrumentation: adaptive optics - galaxies: high-redshift - galaxies: kinematics and dynamics

1 INTRODUCTION

As the current suite of 8 m class telescopes are being pushed to their limits, it is becoming more important to prepare for and define the scientific programmes to be undertaken by the next generation of extremely large telescopes. The European Extremely Large Telescope (E-ELT) is a 39 m diameter telescope being constructed by the European Southern Observatory (ESO) for operations commencing within the next decade. Upon completion, this facility will provide the angular resolution and light gathering power to revolutionise our current understanding in many areas of astrophysics. However, as telescope and instrumentation projects enter such ambitious scales of size and complexity of design, it is becoming imperative to accurately quantify performance prior to construction.

Consequently, several recent integral field spectrograph (IFS) instrumentation projects have developed detailed

instrument simulation models, including KMOS (Lorente et al. 2008), MUSE (Jarno et al. 2008), JWST/NIRSpec (Piqueras et al. 2010; Dorner et al. 2011), and EAGLE/ELT-MOS (Puech et al. 2008, 2010; Puech, Yang & Flores 2010). The most rigorous simulation method involves using the full optical design of the instrument to propagate photons to the detector plane, before using data reduction software to reduce the simulations akin to real data. While this full end-to-end technique is possible for currently operational instruments and those at an advanced stage of design, it is a level above what is required at an early stage of development.

As part of the concept design for an ELT multi-object spectrograph (MOS), Puech, Yang & Flores (2010) developed an IFS instrument simulator that processed input data-cubes, generating mock observation cubes assuming a perfect data reduction process. The simulator encoded all the sky, telescope and adaptive optics (AO; through the point spread function) and instrument parameters, returning mock observations containing source and background flux as well as noise contributions. They were able to anal-

* E-mail: simon.zieleniewski@physics.ox.ac.uk

use the feasibility of a key MOS program to observe star forming galaxies at $z \sim 6$.

The High Angular Resolution Monolithic Optical and Near-infrared Integral field spectrograph (HARMONI) is a proposed instrument selected as one of two first-light instruments by ESO (Thatte et al. 2010). HARMONI is being designed as a single-field, visible and near infra-red (NIR) IFS, and will provide a range of spatial pixel (spaxel) scales and spectral resolving powers, which permit the user to optimally configure the instrument for a wide range of science programs; from ultra-sensitive to diffraction limited, spatially resolved, physical (morphology), chemical (abundances and line ratios) and kinematic (line-of-sight velocities) studies of astrophysical sources. HARMONI will be compatible with two modes of adaptive optics (AO) allowing it to tackle a broad range of problems across astrophysics, including: a) the physics of mass assembly of galaxies at high redshifts, b) resolved studies of stellar populations in distant galaxies, and c) detecting and weighing intermediate mass black holes in nearby galaxies or globular clusters. The full design specifications are listed in table 1. The instrument will commence its preliminary design phase in 2015 and so here we undertake detailed simulations of the performance of HARMONI.

In this paper we present our development of the instrument simulation pipeline HSIM for the HARMONI instrument that will be used to quantify the performance. HSIM improves on the method developed by Puech et al. in several key areas, including spectral line spread convolutions, and a wavelength dependent telescope (plus adaptive optics) point spread function model. We detail the components of HSIM and show the importance of the key stages and their effects on observations. We then showcase the pipeline with two studies: calculations of point source sensitivities for the available observing modes, and a case study of measuring kinematics of star forming galaxies at $z \sim 2-3$.

The paper is organised as follows: Sections 2 and 3 detail the motivation, goals and methodology of the simulations; in Section 4 we present an overview of the pipeline stages; in Section 5 we present our point spread function parameterisation and demonstrate its importance; Section 6 shows our verification crosschecks against existing software; in Section 7 we present predicted point source sensitivities; Section 8 presents our high redshift galaxy simulations; and we finally conclude in Section 9.

Throughout this paper we adopt a flat Λ CDM cosmology with $H_0 = 70 \text{ km s}^{-1} \text{ Mpc}^{-1}$, $\Omega_m = 0.3$ and $\Omega_\Lambda = 0.7$. We use AB magnitudes throughout unless otherwise stated.

2 MOTIVATION AND GOALS

Developing an instrument simulation pipeline serves several important purposes:

- a) it gives a quantitative understanding of the feasibility of observing programs, characterising both the capabilities and limitations of an instrument,
- b) it allows for performance trade-offs between differing instrument designs or configurations.

The first point is important since it will allow observing time on the E-ELT to be more efficiently utilised. Quanti-

fying performance usually consists of determining the exposure time required to achieve a particular signal-to-noise ratio (SNR) for a given target. However, an instrument simulation pipeline allows us to go one step beyond exposure time calculators and ascertain the precision with which we can derive a number of key physical parameters for particular science cases. The input data-cubes can be built to encode as many physical characteristics as desired. The mock output data represents that of real observations and so it is possible to use identical analysis methods as used on real data (or permits users to develop and verify analysis methods prior to taking the real data). This allows the user to specifically determine the feasibility of their science goal (e.g. measuring kinematics, black hole masses, stellar chemical abundances). It also provides a direct comparison between the scientific capabilities of current generation instrumentation and those of the E-ELT era.

Designing a self-contained and modular pipeline means that all simulations are kept consistent within the current design of the instrument. The pipeline can easily be modified to reflect any changes in the instrument design (e.g. changing spaxel scales, spectral resolving power etc), thus allowing exploration of the second point above. It will also be possible to explore instrument effects such as imperfect sky subtraction and spectrograph throughput variations, and give quantitative constraints on such calibration issues. In this paper we concentrate on the accuracy with which physical parameters can be measured for a specific science case.

3 SIMULATION METHODOLOGY

The procedure for performing simulations can be broken down into three parts:

- a) An input data-cube encoding the physical characteristics of the object. This can include properties such as kinematics, absorption/emission lines, dynamics, morphology, chemical abundances etc;
- b) A simulation pipeline that takes the input and adds all the first-order sky, telescope, instrument, and detector effects, as well as random and systematic noise, creating an output mock-observed data-cube. The user is able to choose suitable observing parameters to be able to explore the instrument and telescope modes;
- c) The analysis of the output mock-observed data to enable an understanding of what information can be extracted from the observation, i.e. how well can the properties of the input data-cube be recovered in the output cube.

Within this framework there are two areas of parameter space to be explored: the physical characteristics of the objects (e.g. morphology, mass, redshift, magnitude, line strengths) as well as the observational characteristics of the telescope, and instrument (e.g. spatial scale, exposure time, resolving power, emissivity, AO correction). Consequently the combined parameter space is vast, and a full exploration is simply not possible. For the purposes of this paper, we have firstly pursued point source sensitivity calculations for all current instrument configurations, which gives a general overview of the performance of the instrument design. We then present simulations of a representative case of $z \sim 2-3$ emission-line galaxies.

Table 1. Current design parameters for HARMONI.

Wavelength range	0.47 - 2.45 μm
Spatial scales (FoV)	4 mas ($0.86'' \times 0.61''$), 10 mas ($2.14'' \times 1.52''$) 20 mas ($4.28'' \times 3.04''$), 60 \times 30 mas ($9.12'' \times 6.42''$)
Spectral Resolution (& waveband)	3500 ($V + R$; $Iz + J$; $H + K$) 7500 (Iz ; J ; H ; K) 20000 (half of each NIR band)
Temperature	120 K cryostat, 40 K detectors
Detectors	Teledyne HgCdTe 4k \times 4k for NIR 4k \times 4k CCD for visible
Throughput	Target $\geq 30\%$ average
AO modes	SCAO, LTAO, seeing-limited

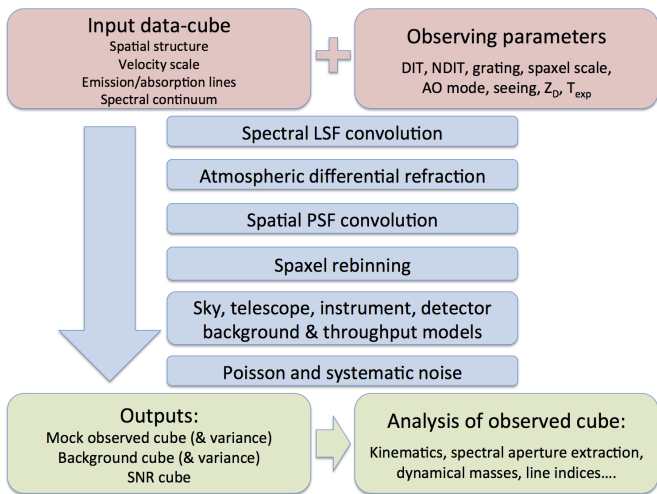


Figure 1. Flowchart of the simulation process. Input data-cubes provide all the physical details of the object. The cube is then ‘observed’ for given instrument, telescope and site parameters. The observing process adds all first-order telescope and instrument effects, as well as random and systematic noise. The output cube represents a perfectly reduced data-cube, and can be analysed exactly like real data.

4 SIMULATION PIPELINE OVERVIEW

We first presented the simulation pipeline in Zieleniewski et al. (2014) and here we provide an overview of each stage, highlighting several novel features. The overall process is presented in Fig. 1. HSIM is written in PYTHON and makes use of the ASTROPY package (Astropy Collaboration et al. 2013), as well as the NUMPY and SCIPY packages. It handles input and output data in FITS format, as this is the usual file format for 3D spectrographs. The input data-cube is uploaded as a 3D array of two spatial and one spectral dimension. The FITS headers contain all the relevant information about the object (e.g. spatial and spectral sampling, flux units, spectral resolution). The user chooses suitable observing parameters and the data-cube is then processed through several steps:

4.1 Line spread function convolution

The spectral resolution of the input cube is degraded to the output resolution depending on the chosen grating. This is achieved by convolving the spectral dimension with a Gaussian line-spread function (LSF). We use a Gaussian of constant full width half maximum (FWHM) as a reasonable approximation for the resolution of a slit-width limited grating spectrometer. We ensure the output resolution of the cube is consistent by generating a LSF of width $\Delta\lambda_{\text{conv}}$ given by

$$\Delta\lambda_{\text{conv}} = \sqrt{(\Delta\lambda_{\text{out}})^2 - (\Delta\lambda_{\text{in}})^2}, \quad (1)$$

where $\Delta\lambda_{\text{in}}$ is the spectral resolution of the input cube specified in the FITS header (by the user), and $\Delta\lambda_{\text{out}}$ is the output resolution given by the chosen grating. The spectral dimension of the cube is then sampled (with a minimum of two pixels per FWHM to approximate the Nyquist limit). If the input spectral resolution is coarser than the grating resolution ($\Delta\lambda_{\text{in}} > \Delta\lambda_{\text{out}}$) then the user can choose to either convolve with a LSF of width $\Delta\lambda_{\text{out}}$ or perform no spectral convolution. The former option is useful in situations where the input data-cube contains a spectrum where the resolution is limited by e.g. stellar velocity dispersion in galaxies, and the spectrum still needs to incorporate the instrumental effect. The option to ignore the spectral convolution is always available if it is not required (e.g. if the input data-cube has been pre-formatted spectrally).

4.2 Atmospheric differential refraction

The effect of atmospheric differential refraction (ADR) is added according to the equations of Schubert & Walterscheid (2000) and Roe (2002). The angle in radians between the true zenith distance Z_D and the apparent zenith distance Z_a is approximated by

$$R = Z_D - Z_a \simeq \left(\frac{n^2 - 1}{2n^2} \right) \tan Z_D, \quad (2)$$

where the refractive index n is a function of wavelength, pressure, temperature and humidity. Thus the angular change $R_1 - R_2$, between two wavelengths is given by:

$$R_1 - R_2 = \left(\frac{n_1^2 - 1}{2n_1^2} - \frac{n_2^2 - 1}{2n_2^2} \right) \tan(Z_D), \quad (3)$$

where n is the refractive index at a given wavelength and Z_D is the zenith distance. This effect is prominent at both

visible wavelengths, where the refractive index varies the most strongly with wavelength, and at the smallest spatial scales. Each wavelength channel (spatial image at a given wavelength in the 3D cube) is shifted relative to an optimal wavelength, which is calculated to give equal shift on either side. The shift is made along the longest spatial dimension of the output data-cube (this assumes the user aligns the longest spatial axis of the instrument field of view along the parallactic angle). After the data-cube is rebinned to the chosen spaxel scale, the ADR is ‘corrected’ by shifting the wavelength channels back again to emulate the correction achieved by a data reduction pipeline. This stage reduces the common field of view of the data-cube. The second order effect whereby the axis of ADR moves throughout an exposure causing the object to blur in the data-cube, is not included.

4.3 Point spread function convolution and spatial rebinning

Each wavelength channel is convolved with an AO spatial PSF. We have developed a novel method for parameterising AO PSFs as detailed in Zieleniewski & Thatte (2013) allowing us to generate PSFs at any wavelength within the HARMONI range. This is described in more detail in Section 5. The pipeline generates PSFs at 1 mas sampling and performs the PSF convolution at a scale of 1/10th of the output spatial scale in order to minimise convolution effects due to the finite sampling of the input cube and PSF. If the input data-cube is coarser than 1/10th of the output scale then it is interpolated up to 1/10th, ensuring flux conservation.

The data-cube is rebinned to the chosen output spatial scale ensuring flux conservation.

4.4 Background and throughput

Total background and throughput cubes are generated incorporating the effects of sky, telescope, instrument and detector. We use the ESO Skycalc sky model described by Noll et al. (2012) and Jones et al. (2013) for both emission and transmission. We model the telescope as a grey-body whereby a thermal black-body curve for the given site temperature is multiplied by a constant emissivity.

4.5 Noise

Poisson noise from the object, sky and telescope background, and detector dark current is added along with detector read-out noise. We use separate statistics to represent the use of CCDs for visible wavelengths and NIR arrays for longer wavelengths. The NIR detector statistics are modelled on the KMOS HAWAII-2RG detectors (Finger et al. 2008) and the CCD statistics based on the MUSE calibration data (D. Ives, priv. comm.).

4.6 Outputs

The final outputs of HSIM are:

1. A mock observed cube: the main product of the simulation containing flux from the source, background and detector

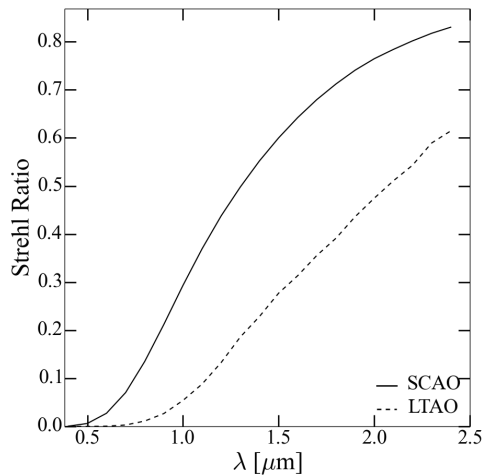


Figure 2. Strehl ratios of parameterised PSFs used in HSIM as a function of wavelength for SCAO (solid lines) and LTAO (dashed lines). PSFs are generated at a seeing of $0.67''$ and sampling of 1 mas. Both the smooth variation of AO performance and the improved performance at longer wavelengths are evident.

along with all associated noise for each (x, y, λ) pixel of the cube;

2. A background cube containing all background flux;
3. A SNR cube giving the signal-to-noise ratio for each pixel calculated as

$$SNR = \frac{O(x, y, \lambda)T_{\text{exp}}\sqrt{N_{\text{exp}}}}{\sqrt{O(x, y, \lambda)T_{\text{exp}} + B(x, y, \lambda)T_{\text{exp}} + D \cdot T_{\text{exp}} + \sigma_{\text{R}}^2}}, \quad (4)$$

where $O(x, y, \lambda)$ is the object counts per second for a pixel in the 3D cube, $B(x, y, \lambda)$ is the total background counts per second, D is the total dark current per second, σ_{R} is the read-out noise, T_{exp} is the exposure time in seconds and N_{exp} is the total number of exposures.

There are also options to return a noiseless object cube containing only source flux, return a transmission cube, and perform automatic perfect sky subtraction (observed cube - background cube).

5 EFFECTS OF THE AO POINT SPREAD FUNCTION

The effects of the telescope and AO system on observations are encoded in the spatial PSF. The E-ELT PSF is predicted to be a strong function of wavelength as well as other parameters including seeing, off-axis distance from reference AO star, and guide star magnitude. Its complex form means it needs to be incorporated carefully into the simulations not simply modelled as a simple Gaussian or Moffat function. We have incorporated a continuously varying AO PSF as a function of wavelength and seeing, for both LTAO and SCAO, in our simulation pipeline, using the *eltpsf* program developed by J. Liske¹. This allows the user to fit a 1D average radial profile of a PSF with a set of analytical functions. We used a set of simulated long-exposure LTAO and SCAO

¹ https://www.eso.org/sci/facilities/eelt/science/drm/tech_data/ao/psf_fitting/ - last accessed 01-06-15

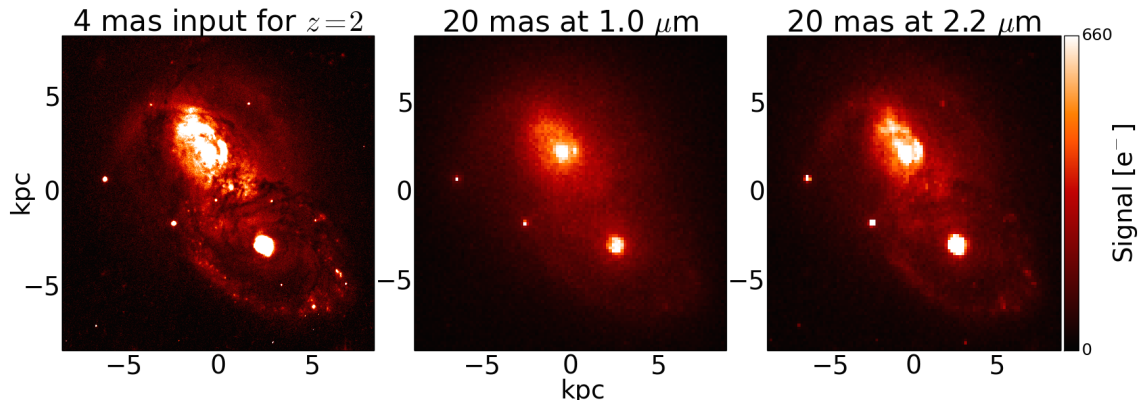


Figure 3. Integrated continuum maps from an HSIM simulation of a ULIRG observed with LTAO. Left panel shows the input map at a sampling of 4 mas after scaling an *HST* WCS image of a local galaxy (50 mas sampling) to the correct spatial extent at $z = 2$. Centre panel shows a 20 mas continuum map at $1.0 \mu\text{m}$ in the *Iz*-band. Right panel shows a continuum map at $2.2 \mu\text{m}$ in the *K*-band. The observed maps are shown at $\text{SNR} = 10$. We assume identical intensity and spatial distribution for both continuum maps. The improved PSF performance at longer wavelengths is clearly evident.

PSFs (T. Fusco & N. Schwartz, priv. comm.), covering the HARMONI wavelength range, and fitted each of these with a combination of an obscured Airy function, Moffat function and Lorentz function (Zieleniewski & Thatte 2013). Interpolating the parameters of each analytical function with wavelength, we then obtain the PSF at each wavelength. We have so far only used on-axis PSFs and we assume the PSF does not vary spatially within the field of view. Fig. 2 shows the measured Strehl ratios of our parameterised PSFs for both LTAO and SCAO. The smooth variation of AO performance with wavelength in our parameterised PSFs is clear.

The importance of the wavelength variation is worth emphasising. Whilst the diffraction limit of a telescope increases from visible to NIR wavelengths, AO performance vastly improves at longer wavelengths because the atmospheric turbulence becomes relatively less disruptive. This large improvement, as seen in Fig. 2, more than compensates for the increasing diffraction limit at longer wavelengths. We demonstrate this qualitatively in Fig. 3, which shows two continuum maps of a simulated HARMONI observation of an ultra luminous infra-red galaxy (ULIRG) at a redshift of $z = 2$. The input *HST ACS* image at a resolution of 50 mas (IRAS06076-2139: from Armus et al. 2009) has been scaled spatially to 4 mas at $z = 2$. The left map shows the object as observed in the *Iz*-band at $1.0 \mu\text{m}$. The right map shows the object as observed in the *K*-band at $2.2 \mu\text{m}$. For easier comparison we assume equal flux at both wavelengths and we ignored the increased thermal background in the *K*-band. It is clear from the two maps that the spatial resolution in the *K*-band is much improved over the *Iz*-band, providing exquisite detail of the underlying star-forming morphology of the ULIRG.

The AO PSFs that we used for the parameterisation also include a small amount of intrinsic jitter or blur, which estimates the effect of wind-shake jitter on the telescope structure. This corresponds to 2 and 3 mas rms for the SCAO and LTAO PSFs respectively. We include the ability to add additional amounts of PSF blur to approximate reduced AO performance. We model this by convolving the AO PSF with a Gaussian of chosen rms width, so any additional blurring adds in quadrature.

6 VERIFICATION RUN

To test the results of HSIM we compare to two separate tools. Firstly, we compared to the pipeline of Puech et al. (2010), which has itself been verified using real SINFONI observations from Genzel et al. (2006). As part of the E-ELT design reference mission (DRM) science case C10: *The physics and mass assembly of galaxies out to $z \sim 6$* , Puech et al. undertook simulations of which some examples are publicly available². We took the example data-cube UGC5253, a rotating disc galaxy with prominent $\text{H}\alpha$ emission.

We converted the cube for compatibility with our pipeline using the description from the DRM. We then ran simulations using identical parameters as used by Puech et al. including the identical spatial PSF. The only difference between the two runs is that Puech et al. do not specify the sky transmission spectrum they use, so we manually convolved one from the E-ELT DRM to match the spectral resolution of the data-cube.

The outputs of the comparison are shown in Fig. 4. Our pipeline computes the total signal of N_{exp} combined exposures, so we have divided our output cube by N_{exp} to get a mean value for each pixel (cf. Puech et al. who determine the median value of each pixel from N_{exp} cubes). It is clear from both the signal and SNR plots that we are computing consistent values within the uncertainty of different transmission functions, and can be confident that our pipeline is working correctly.

For the second crosscheck we compared our pipeline with the ESO SINFONI exposure time calculator (ETC). We ran the ETC for an extended object with an A0V spectrum at a *K*-band Vega magnitude of 14, observed with no adaptive optics for two hours ($8 \times 900\text{s}$). The ETC returns the input spectrum which we used to create an input cube. We simulated an identical observation with HSIM, using a Gaussian PSF and the relevant VLT telescope parameters. We were careful to calculate our object flux over two spatial pixels as done by the ETC. We note that we approximated the

² <https://www.eso.org/sci/facilities/eelt/science/drm/C10/> - last accessed 01-06-15

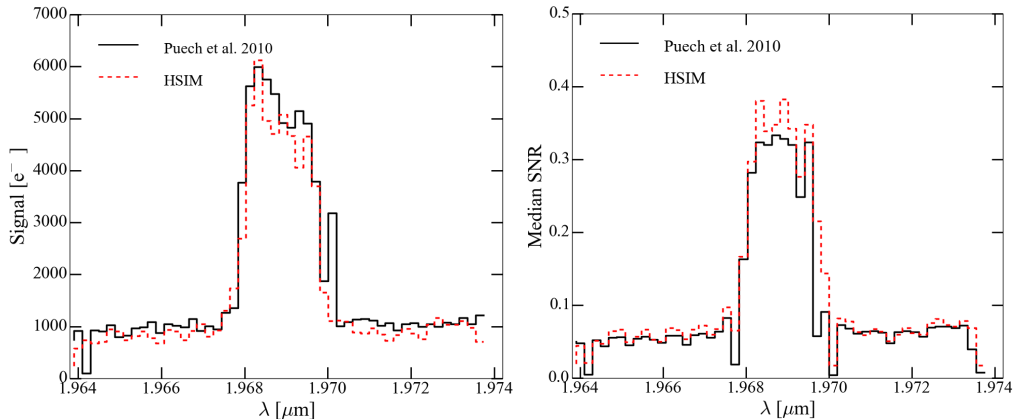


Figure 4. Left: comparison of the signal extracted from a 10 spaxel radius aperture centred on the galaxy between Puech et al. simulation and HSIM. Right: comparison of the median SNR over every spaxel in each wavelength channel. The simulations are consistent to within the noise realisations.

output resolution of our spectrum using the central wavelength value of the spectrum divided by the resolving power of the SINFONI grating, as it is unclear exactly how the LSF convolution is performed in the ETC. We show the results of a comparison in Fig. 5. The two main panels show the total SNR and object signal within two spaxels. The two smaller panels show the respective residuals after median smoothing by 10 spectral pixels to account for potential differences in LSF convolution. Our results show extremely good agreement with the ETC with sub 5 per cent residuals over the majority of the spectrum (the largest residuals appearing at the blue end of the spectrum where the flux values are very small and edge effects occur). This gives us further confidence that our pipeline is working correctly and is producing realistic signal and noise values.

7 SENSITIVITY PREDICTIONS

In this section we present instrument point source sensitivities for several operating configurations of HARMONI as computed using HSIM. We compute the limiting AB magnitude M_{AB} to achieve $SNR = 5$ per spectral resolution element (2 pixels) after five hours on source ($T_{exp} = 900$ s). We assume sky subtraction with no penalty to on-source exposure time, using ‘nodding-on’ or similar techniques. To do this we calculate the SNR for a given M_{AB} after 5 hours on source, then compute the multiplicative factor f required to give a M_{AB} that yields $SNR = 5$. Adding this factor (and extra factors for sky subtraction and summing over two spectral pixels) equation 4 becomes

$$SNR = \frac{f \cdot O \cdot T_{exp} \sqrt{N_{exp}} \sqrt{2}}{\sqrt{(f \cdot O + 2B + 2D) \cdot T_{exp} + 2\sigma_R^2}}, \quad (5)$$

and this is solved for f using the standard quadratic equation where the negative solution is discarded. The SNR is calculated within a 2×2 spaxel extraction aperture, although for the 30×60 mas scale we upsize to a 120×120 mas box. We compare R , H and K bands. For each band we create an input cube containing a point source with a flat spectrum (constant M_{AB}). The input cubes are generated with a spatial sampling of 0.4 mas for the 4×4 mas output scale and at

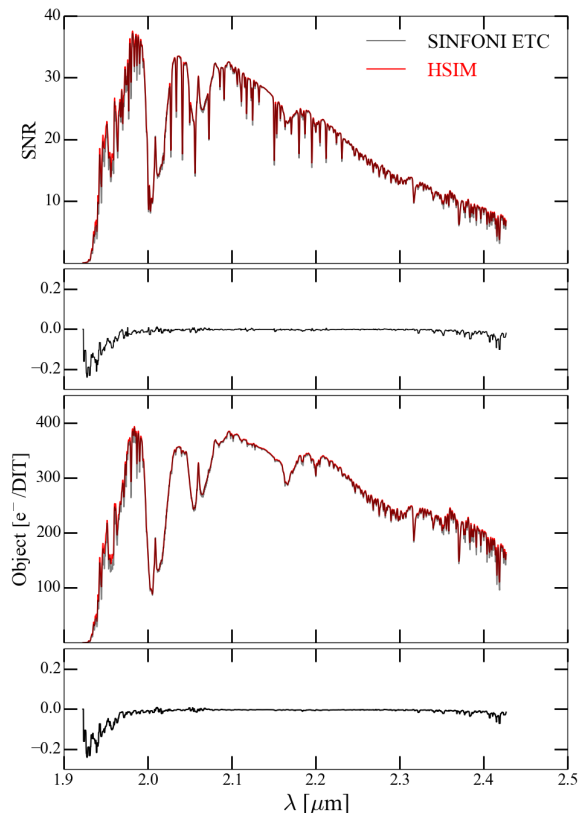


Figure 5. Comparison of the total SNR and object signal between HSIM (red) and the SINFONI ETC (grey). The two main panels show the total SNR and object signal within two spaxels. The two smaller panels show the respective residuals after median smoothing by 10 spectral pixels.

1 mas for the 10×10 , 20×20 and 30×60 mas output scales. The input cube is generated with ~ 30 wavelength channels so as to be computationally efficient. The SNR is an average value over all the wavelength channels in the spectrum extracted from the 2×2 spaxel box. For each grating we choose wavelength regions minimally affected by sky lines and telluric absorption. The central wavelengths for each

input cube are $0.677\ \mu\text{m}$ for R -band, $1.76\ \mu\text{m}$ for H -band, and $2.145\ \mu\text{m}$ for K -band.

These sensitivity calculations are intended to provide a general indication of the performance of the current instrument design. Whilst the instrument parameters (e.g. throughput, dark current, read-out noise) are not set at the minimum specification, we use simple 2×2 spaxel aperture extraction to present reasonably conservative performance estimates. Improved SNR would be obtained using the more rigorous method of optimal extraction (Horne 1986; Robertson 1986).

7.1 Simulation parameters

We set the following instrument and site parameters as to provide conservative estimates for the resulting performance.

Site and telescope: We use a Paranal-like site (and telescope) temperature of $280.5\ \text{K}$. Seeing is set to the Cerro Armazones median value of $0.67''$ FWHM at $0.5\ \mu\text{m}$. We use the official 39 m E-ELT model, which has a maximum all-glass diameter of 37 m, an obscuration ratio of 0.3 and six spider arms, giving a total collecting area of $A = 932.5\ \text{m}^2$. We use an emissivity of 0.244 motivated by the current telescope design of seven warm reflections (5 mirror E-ELT + 2 further mirrors into HARMONI on the Nasmyth platform) of protected silver and aluminium (MgF_2 on $\text{Ag}+\text{Al}$) coated mirrors and six unmasked spider arms.

Instrument: We use an instrument throughput of 35 per cent. The operating temperature of $120\ \text{K}$ means the instrument contributes negligible thermal background.

Detector model: The NIR detector statistics are modelled on the KMOS HAWAII-2RG detectors (Finger et al. 2008). We use a dark current value of $0.0053\ \text{e}^- \text{s}^{-1} \text{pix}^{-1}$ and read-out noise of $2.845\ \text{e}^- \text{pix}^{-1}$. For the visible CCD detector statistics we adopt a dark current of $0.00042\ \text{e}^- \text{s}^{-1} \text{pix}^{-1}$ and read-out noise of $2.0\ \text{e}^- \text{pix}^{-1}$. The wavelength cut between visible and NIR detectors is set at $0.8\ \mu\text{m}$.

7.2 Results

We present the results of sensitivities for LTAO observations in tables 2 and 3. Table 2 gives the estimated limiting magnitudes to achieve $\text{SNR} = 5$ measured from a 2×2 spaxel aperture (4×2 for the $30 \times 60\ \text{mas}$ scale). These are separated into visible R -band, and NIR H and K bands and for each resolving power. In the R -band sensitivity increases with spaxel size. AO performance at visible wavelengths is poor, with Strehl ratios of ~ 1 per cent, so larger spaxels incorporate more object flux. In the H -band the $20 \times 20\ \text{mas}$ scale offers slightly improved sensitivity compared to the $10 \times 10\ \text{mas}$ scale and $\sim 1\ \text{mag}$ greater sensitivity compared to the $4 \times 4\ \text{mas}$ scale. However, in the K -band, the $10 \times 10\ \text{mas}$ is $\sim 0.4\ \text{mag}$ more sensitive than the $20 \times 20\ \text{mas}$ scale. This is due to the increased thermal background in K -band, which penalises the larger spaxel scales. We also perform identical simulations for SCAO and seeing-limited observations. We find that SCAO results in $\sim 0.6\ \text{mag}$ better sensitivity in H -band and $\sim 0.4\ \text{mag}$ improvement in K -band. R -band observations with SCAO are not possible due to the visible light being used for AO correction. Seeing-limited limiting magnitudes are $\sim 1.5\ \text{mag}$

Table 2. Point source sensitivity predictions for HARMONI with LTAO calculated from a 2×2 spaxel aperture centred on the object.

2 × 2 spaxel aperture					
Band	R	4 × 4	10 × 10	20 × 20	30 × 60
R	3500	22.7	23.6	24.3	25.1
H	3500	26.2	27.0	27.0	26.4
	7500	25.2	26.0	26.1	25.7
	20000	24.1	25.0	25.1	24.9
K	3500	25.7	26.3	25.8	24.8
	7500	25.2	25.8	25.4	24.5
	20000	24.2	25.1	24.8	23.9

Notes: Limiting AB magnitudes to achieve $\text{SNR} = 5$ per spectral resolution element for five hours on-source ($T_{\text{exp}} = 900\ \text{s}$). We assume sky subtraction with no penalty to on-source exposure time. Band column gives the bandpass region, R is the resolving power and the remaining columns give the limiting magnitude for each HARMONI spaxel scale. 4×2 spaxel aperture for $30 \times 60\ \text{mas}$ scale.

Table 3. Point source sensitivity predictions for HARMONI with LTAO calculated from a square aperture that encloses 50 per cent of the ensquared energy (EE) for each band.

50 per cent EE square aperture					
Band	R	4 × 4	10 × 10	20 × 20	30 × 60
R	3500	23.6	24.6	25.1	25.4
H	3500	24.5	25.4	26.0	26.2
	7500	23.5	24.5	25.1	25.6
	20000	22.5	23.4	24.1	24.7
K	3500	24.7	25.1	25.1	-
	7500	24.1	24.6	24.8	-
	20000	23.1	23.9	24.2	-

Notes: Limiting AB magnitudes to achieve $\text{SNR} = 5$ per spectral resolution element for five hours on-source ($T_{\text{exp}} = 900\ \text{s}$). For the R , H and K bands the 50 per cent EE apertures correspond to 400×400 , 140×140 and $80 \times 80\ \text{mas}$ respectively. We assume sky subtraction with no penalty to on-source exposure time. Band column gives the bandpass region, R is the resolving power and the remaining columns give the limiting magnitude for each HARMONI spaxel scale.

lower than LTAO for R -band at the $30 \times 60\ \text{mas}$ scale and $\sim 2.5\ \text{mag}$ lower for H and K -bands.

Table 3 shows magnitudes for identical observations as table 2 but after extracting the spectrum from an aperture containing 50 per cent of the ensquared energy of the PSF. For the R , H and K bands these correspond to 400×400 , 140×140 and $80 \times 80\ \text{mas}$ respectively. We omit values for the $30 \times 60\ \text{mas}$ spaxel scale in K -band because the 4×2 spaxel aperture already contains greater than 50 per cent of the ensquared energy. This table shows that a greater SNR can be achieved in the R -band by increasing the aperture size. For the 4×4 and $10 \times 10\ \text{mas}$ scales, a factor of $\sim 1\ \text{mag}$ improvement is gained. However, for both H and K bands, the limiting magnitudes are lower because the extra spaxels from the larger extraction aperture contribute more detector noise, as can be seen from Figs 6 and 7.

To illustrate the different noise regimes, Figs 6 and 7

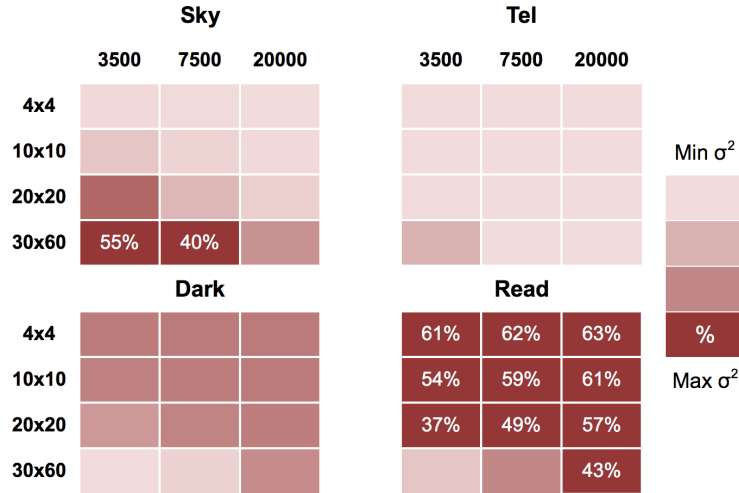


Figure 6. Heat map showing contributions to the variance for LTAO point source observations in H -band for five hours on source ($T_{\text{exp}} = 900$ s) after extracting in a 2×2 spaxel aperture centred on the object. The four quadrants show the contributions to the variance from (clockwise from top left) sky, telescope, read-out noise and dark current respectively for each observing mode of the instrument (spaxel scale and resolving power). The instrument thermal background is assumed to be negligible. Dark colours show a greater contribution and light colours show a smaller contribution. For each instrument configuration, the box with the greatest contribution contains its percentage contribution to the total variance. Observations in H -band are predominately read-out noise limited except at the coarsest spaxel scale and lowest resolving powers which are sky limited.

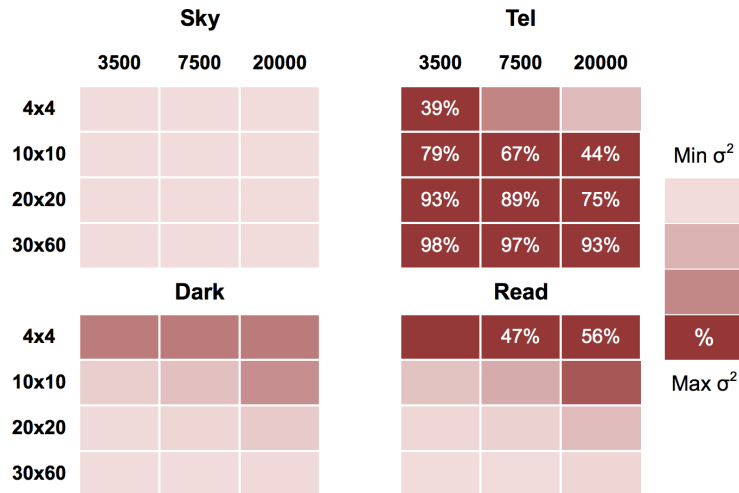


Figure 7. Same as Fig. 6 but for K -band observations: heat map showing contributions to the variance for LTAO point source observations in K -band for five hours on source ($T_{\text{exp}} = 900$ s) after extracting in a 2×2 spaxel aperture centred on the object. Comparing to Fig. 6 the K -band observations are dominated by the telescope thermal background, except at finest spaxel scale and highest resolving powers which are read-out noise limited.

show heat maps representing the contributions to the total variance from each source: sky, telescope, dark current, and read-out noise, when observing with LTAO in the H -band and K -band respectively. Each observing configuration is represented by a single box. Light colours show small contribution and dark colours show larger contribution. For each observing configuration, the box with the largest contributor contains the percentage of the total variance from that source. It is clear from these figures that in H -band HARMONI is generally detector read-out noise dominated, except for the configuration of 30×60 mas scale combined with the two lowest resolving powers, which are sky dominated.

However, in the K -band observations are telescope (thermal) background dominated, except for the finest spaxel scale and highest resolving powers.

8 CASE STUDY: SIMULATIONS OF EMISSION-LINE GALAXIES AT $Z \sim 2 - 3$

One of the major science goals of HARMONI is to spatially resolve the interstellar medium (ISM) of high-redshift ($z \sim 2-5$) galaxies and measure the physical processes occurring on scales of individual HII regions. At these red-

shifts, the comoving star-formation density was substantially higher than at $z \sim 0$, and so this era has been heralded as the peak epoch of galaxy formation when most of today's massive galaxies formed the bulk of their stellar mass (Madau & Dickinson 2014). At these early times, the Hubble sequence was not in place, and galaxies appear to be undergoing significant changes to their morphologies and stellar populations. Over the past decade major advances have been made in measuring the dynamics of galaxies at this epoch using integral field spectroscopy (e.g. SINS: Genzel et al. 2006, Förster Schreiber et al. 2006, 2009; OSIRIS: Law et al. 2007, 2009; KMOS: Wisnioski et al. 2015; see also Glazebrook 2013 review). However, due to the photon-starved nature of the observations, deriving the dynamics of high redshift galaxies requires long integration times, and only offers limited spatial resolution. Moreover, even with natural- or laser-guide star AO assisted observations, spatially resolved studies are limited to $\gtrsim 1$ kpc resolution (e.g. Förster Schreiber et al. 2011a,b; Swinbank et al. 2012b,a). Gravitationally lensed star-forming galaxies do provide the unique ability to resolve regions at scales of ~ 60 – 200 pc (Jones et al. 2010; Livermore et al. 2012, 2015), however these are notable rare exceptions limited to a handful of objects.

The increased light grasp and spatial resolution of the E-ELT should allow the study of high-redshift galaxies on the scales of individual star forming HII regions (down to 100 pc scales). The properties (e.g. sizes, luminosities, velocity dispersions, chemical make-up, and spatial distribution) of HII regions reflect the underlying ISM (such as gas density and pressure), which in turn reflect the dominant route by which galaxies accrete the bulk of their gas.

The goals of the simulations presented in this section are to investigate the ability to detect and measure kinematics of emission-line galaxies at redshifts of $z \sim 2$ – 3 , using HARMONI on the E-ELT. Our goals are to:

- (i) determine how well the global kinematics (e.g. rotation curves) can be derived as a function of star-formation rate, size and morphology for galaxies at $z \sim 2$ – 3 ;
- (ii) determine the smallest physical scales for which physical properties can be derived, including identifying / measuring the properties of individual star forming regions.

To demonstrate the use of our simulation pipeline in this area, we present results from a set of simulated observations of a sample of emission-line galaxies at $z \sim 2$ – 3 . We focus on galaxies with prominent H α emission, which falls into the K -band at these redshifts. We highlight that our simulations are not designed to test galaxy formation models. Rather they are designed to test how well measured properties (e.g. rotation curves, clump properties) can be derived for a given exposure time (or at a given spatial resolution) using a reasonable input galaxy image/spectrum with a set of disc and clump scaling relations.

In the rest of this section, we discuss how we construct mock data-cubes, our simulation runs, analysis methods and derived conclusions for this science case.

8.1 Input data-cubes

We generate a sample of input galaxy data-cubes covering a range of star formation rates, redshifts and morphologies ranging from smooth exponential discs of gas and stars to

‘clumpier’ galaxies (gas follows stars in each case). Each galaxy datacube is generated with values randomly picked from a range of uniformly distributed physical parameters: redshift (2.05–2.8), total disc star formation rate SFR (1 – $200 M_{\odot} \text{ yr}^{-1}$), gas fraction (0.1–0.9), inclination (20–70 deg), position angle (0–360 deg), reddening A_v (0–1.5 mag), half-light radius r_{hl} (0.5–2.5 kpc), disc intrinsic velocity dispersion (15 – 40 km s^{-1}) and metallicity ($Z = 0.05$ – $1 Z_{\odot}$). The underlying light profile of the galaxy disc follows an exponential profile, and the velocity field follows a simple *arctan* model (Courteau 1997). We use the star formation law of Kennicutt (1998). We also add a number of star-forming regions using scaling relations inferred from observations of lensed star-forming galaxies at $z \sim 1$ – 3 (e.g. Jones et al. 2010; Livermore et al. 2012, 2015). The number of star-forming clumps is set using the redshift dependent clump luminosity function from Livermore et al. (2012, 2015), where the normalisation is a function of the disc gas fraction and ranges from 0.01–2. The clump velocity dispersion and sizes use the scaling relations from Livermore et al. (2015).

Finally, we include stellar continuum assuming either a constant or exponential star formation history (with an integral that matches the dynamical mass after accounting for gas fraction). We use a solar metallicity simple stellar population model with a Chabrier (2003) initial mass function to derive the stellar continuum and assign this to the disc according to its luminosity profile.

For the purposes of this analysis, we generate input cubes with a spatial sampling of 10×10 mas and a resolving power of $R = 10,000$.

8.2 Simulation runs

We simulate a series of mock HARMONI observations of these galaxies using LTAO. We adopt $T_{\text{exp}} = 900$ s and use the $R \sim 3500 H + K$ grating. We focus on simulations at 20×20 mas (~ 200 pc at $z = 2$ – 3) scales unless otherwise stated. The pipeline parameters (site, telescope, instrument and detector) are all set identically to those used for the sensitivity calculations (see section 7.1).

8.3 Global kinematic measurements

In Fig. 8 we show the recovered H α flux distribution and gas kinematics for a sample of five smooth-disc galaxies assuming a 10 hour integration. We use a Gaussian fitting routine to fit the H α (and NII) emission lines spaxel-by-spaxel. This routine iterates over each spaxel and fits both the continuum and Gaussian profiles to the spectrum. In cases where no fit is made we average over the surrounding spaxels to increase signal at the expense of spatial resolution. For the velocity maps, which show the global gas kinematics, we bin over a 3×3 spaxel box, giving a varying resolution of 20 mas in the bright regions to 60 mas in fainter regions. We use a SNR threshold of 7 for detection of an emission line.

From Fig. 8 we see that HARMONI is capable of measuring velocity profiles in galaxies down to Milky Way-like star-formation rates on scales of at least ~ 200 pc (in the brightest/highest SNR regions) in this integration time. In Fig. 9 we show the rotation curves for galaxy B (extracted along a ~ 1 kpc wide slit aligned along the semi-major axis)

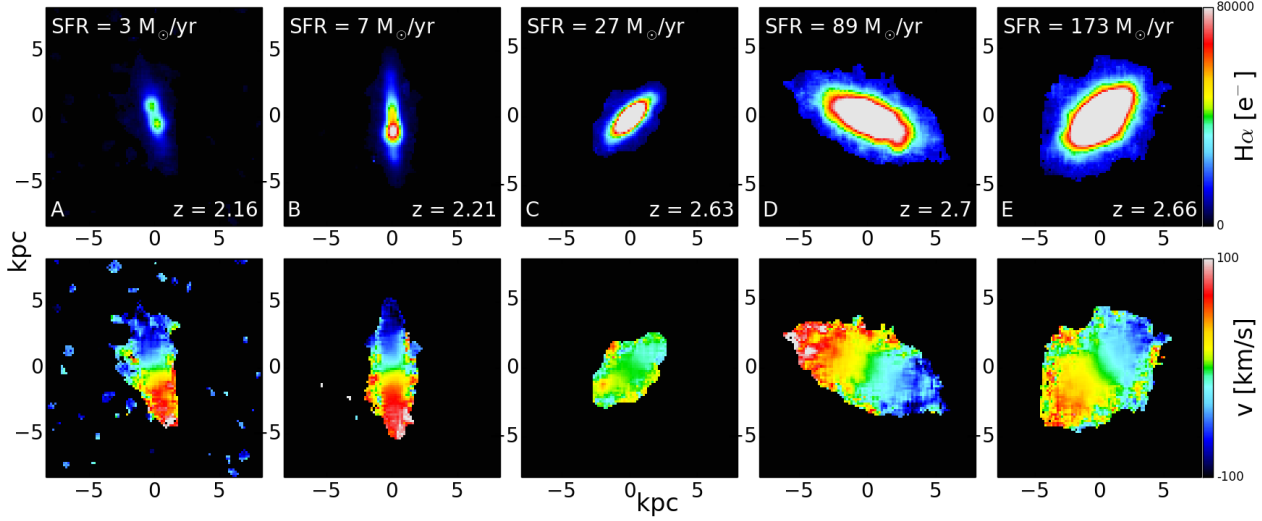


Figure 8. Maps of H α flux (top row) and line-of-sight velocity (bottom row) for smooth disc galaxies. Galaxies are ordered in increasing SFR from left to right. Also shown is the redshift of each galaxy. All galaxies are observed for 10 hours at the 20×20 mas (~ 200 pc) scale. Velocity gradients are easily measured even for the lowest SFRs with a factor of ~ 5 improvement over existing instruments in the highest SNR regions.

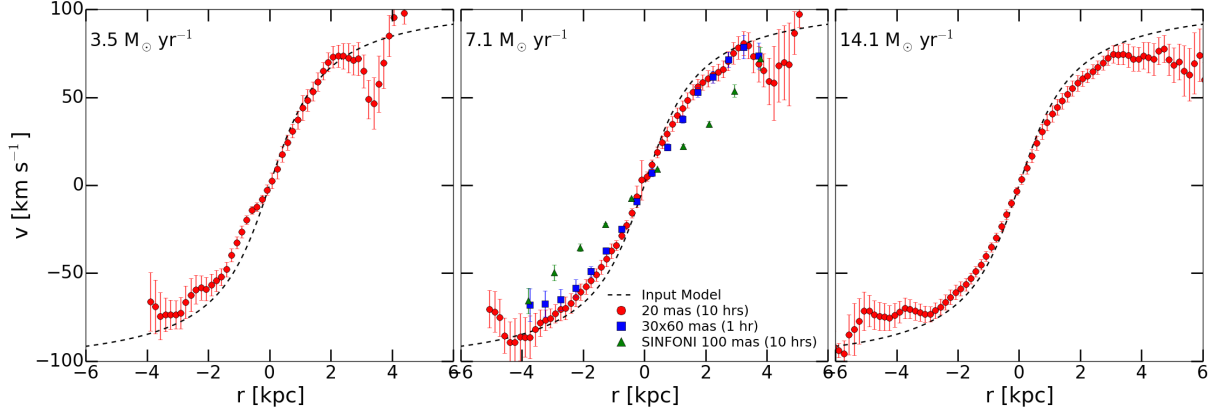


Figure 9. Rotation curves for smooth disc galaxy B with varying SFR (increasing left to right) at 20 mas scale (red circles) as observed by the E-ELT with HARMONI. The input model curve is shown as the dashed black line. Also plotted in the centre subplot is the rotation curve for a 1 hour observation at the 30×60 mas scale (blue squares), which has been binned up to 60 mas spaxels. We also show a simulated 10 hour VLT (SINFONI) observation at 100 mas (green triangles). All curves are extracted along a ~ 1 kpc slit aligned along the semi-major axis. From these simulations the E-ELT with HARMONI offers a 10 fold improvement in observing efficiency compared to current telescopes, i.e. the E-ELT could observe 10 times as many objects in equal observing times. It also offers finer resolution, with $5\times$ more independent data points at the 20 mas scale, and improved sensitivity for equal observing times on the same object

for the same galaxy properties, but with a star-formation rate of $3.5, 7$ and $14 M_{\odot} \text{ yr}^{-1}$ (increasing left to right). This galaxy has the steepest rotation velocity from our sample so gives the best indication of which regions can be recovered for a small range of quiescent star-formation rates. It also shows the effect limited spatial resolution can have on tracing the inner part of the rotation curve (‘beam smearing’). The velocity profile is traced very closely by HARMONI at 20 mas sampling through the central part of the galaxy for all SFRs. The half-light radius of this galaxy is $r_{\text{hl}} = 1.3$ kpc so the curve is recovered out to $3r_{\text{hl}}$ for an SFR of $3.5 M_{\odot} \text{ yr}^{-1}$, which increases to $4.6r_{\text{hl}}$ for a four-fold increase in SFR.

In Fig. 9 we also show the rotation curve for a 1 hour

E-ELT (HARMONI) observation at the coarser 30×60 mas scale (blue squares), which has been binned up to 60 mas spaxels. Comparing this to the rotation curve derived from a simulated 10 hour VLT (SINFONI) observation at 100 mas we see that the E-ELT offers higher resolution data at better sampling with $10\times$ greater efficiency in observing time. For equal observing time the VLT curve underestimates the true curve at all radii and also only extends to $3r_{\text{hl}}$, compared with $4.2r_{\text{hl}}$ from HARMONI at 20 mas sampling. Deriving a simple dynamical mass estimate from each observation gives $\sim 9 \times 10^9 M_{\odot}$ from E-ELT (HARMONI) and $\sim 4 \times 10^9 M_{\odot}$ from the VLT (SINFONI) simulation. Comparing to the input value of $8.6 \times 10^9 M_{\odot}$ this represents both an accurate estimate and a factor of 2 improvement by HARMONI af-

ter 10 hours observing. From these simulations we find that the E-ELT with HARMONI offers a 10 fold improvement in observing efficiency compared to current telescopes, i.e. the E-ELT could observe 10 times as many objects in equal observing times. It also offers improved sensitivity and finer resolution, with $5\times$ more independent data points at the 20 mas scale, for equal observing times on the same object.

8.4 Detailed kinematics

The fine spatial sampling of HARMONI coupled with LTAO will allow for very detailed observations of $z \sim 2$ galaxies. In Fig. 10 we show the observed $H\alpha$ intensity and velocity dispersion maps for the clumpy galaxies in our simulations. To maintain the high spatial resolution required for detecting individual star forming regions we bin over a 2×2 spaxel box where no fit is made to the emission lines, giving an effective resolution of 40 mas (~ 300 pc) in fainter regions, and again use a SNR threshold of 7 for detection of an emission line. As Fig. 10 shows, detailed structure is seen in both the $H\alpha$ emission maps and σ maps. The maps of galaxy J in Fig. 10 (far right) show structure of ~ 3 spaxels in diameter. Thus HARMONI will be able to make very detailed measurements of galaxy substructure, even for galaxies with Milky Way star-formation rates.

To demonstrate HARMONI's ability to discern properties of individual star forming regions, we focus on the galaxy with the lowest star-formation rates from the 'clumpy' galaxy simulations (galaxy F in Fig. 10). Fig. 11 shows the recovered $H\alpha$ signal-to-noise maps for a 10 hour observation at the 20×20 mas (top row) and 10×10 mas (bottom row) scales. For star-formation rates below $10 M_{\odot} \text{ yr}^{-1}$ the 20 mas scale offers superior signal-to-noise, while still resolving individual clumps. However, at a star-formation rate of $1 M_{\odot} \text{ yr}^{-1}$ no clumps are detected with a $SNR > 5$ at the 20 mas scale in 10 hours.

To quantify the likely detection and properties of the clumps in a HARMONI observation we use the 2D CLUMPFIND routine by Williams, de Geus & Blitz (1994) to determine positions and sizes of individual clumps. This method has been used previously by Livermore et al. (2012, 2015) on observations of lensed galaxies. The routine uses isophotes to define clumps starting in the brightest regions and then moving down through the isophote levels. Any isolated contours are defined as new clumps, and any which enclose an existing peak are allocated to that clump. A contour which encloses two or more existing peaks has its pixels divided between them using a 'friends-of-friends' algorithm. We follow a similar procedure as used in Livermore et al. (2015) and set the minimum threshold at 3σ and move up in 1σ steps.

In galaxy F we detect three clumps (indicated by yellow circles on Fig. 11), and proceed to calculate their luminosities and then star-formation rates by summing the pixels within the clump from the $H\alpha$ map (corrected for local background from the underlying disc). We measure star-formation rates in these three clumps to be 1.46 ± 0.02 , 0.26 ± 0.01 and $0.23 \pm 0.01 M_{\odot} \text{ yr}^{-1}$, where the uncertainties are derived from the $H\alpha$ variance map. As a crosscheck of our method we integrate the complete observed $H\alpha$ map and calculate the total star-formation rate of the galaxy to

be $4.12 \pm 0.03 M_{\odot} \text{ yr}^{-1}$ (which is similar to the input value of $4.35 M_{\odot} \text{ yr}^{-1}$).

Finally, assuming the clumps have circular symmetry, we infer a radius of each clump. We measure the radii as 980 ± 150 , 500 ± 200 and 520 ± 250 pc respectively. These match closely to the input clump sizes of 1000, 630 and 500 pc respectively. Comparing these measurements to observations of lensed galaxies (Fig. 9 of Livermore et al. 2015) we see that HARMONI will be capable of detecting and measuring properties of clumps at least a factor 2 smaller than currently possible for normal (unlensed) galaxies at $z \sim 2$ (~ 500 pc compared to ~ 1 kpc). Thus, it should be possible to observe the same galaxy at the 10 mas scale for a greater number of hours and measure properties of even smaller clumps. In fact, from the signal-to-noise map of galaxy F with $SFR = 10.2 M_{\odot} \text{ yr}^{-1}$ in Fig. 11, we see there are clumps of three pixels diameter in the 20 mas scale with $SNR > 5$. This corresponds to ~ 250 pc. Our current analysis is a first step to showcase the capabilities of the simulation pipeline, and we will undertake a more thorough analysis of HARMONI's ability to detect and measure star forming clumps in a follow-up paper.

9 CONCLUSIONS

We present HSIM: a new simulation pipeline for the HARMONI integral field spectrograph on the E-ELT. The pipeline takes input data-cubes and simulates observations, folding in sky, telescope, instrument and detector parameters to create output mock data. HSIM is able to provide quantitative measures of the precision with which we can derive a number of key physical parameters for particular science cases. It allows the user to gain an understanding of the uncertainties associated with making a specific astrophysical measurement. We have described HSIM and presented two studies: point source sensitivity estimates and simulations of $z \sim 2-3$ emission-line star forming galaxies. Our main conclusions are as follows:

1. The E-ELT AO PSF is predicted to be a strong function of wavelength. We show the importance of incorporating this into our simulations. We use a novel parameterisation method to create specific PSFs at each wavelength of the data-cube, which then is convolved with its corresponding data-cube channel.

2. HSIM has been thoroughly crosschecked with existing implementations for other instruments, including the pipeline of Puech, Yang & Flores (2010) and the ESO SINFONI exposure time calculator, and these are consistent with our code.

3. We derive point source sensitivity estimates for observations with HARMONI using LTAO. The 20 mas scale offers the greatest point source sensitivity in H -band, but the 10 mas scale is more sensitive in K -band due to the increased thermal background. We also show that H -band observations are predominately read-out noise limited, whereas K -band is strongly thermal background limited.

4. We perform simulations of $z \sim 2-3$ star forming emission-line galaxies and find that the E-ELT with HARMONI will be capable of obtaining velocity maps of these galaxies down to Milky-Way SFRs at these redshifts, with a factor ~ 5 improvement in spatial resolution over current

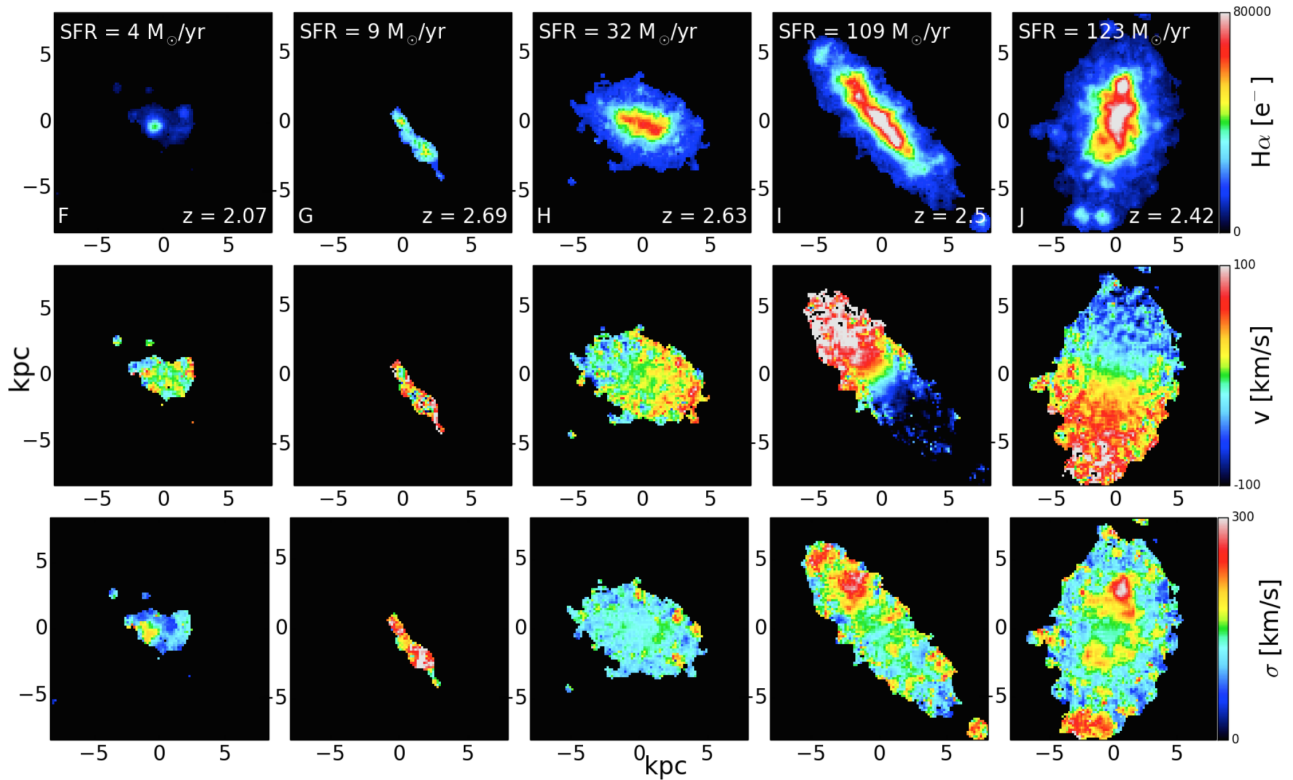


Figure 10. Maps of $H\alpha$ flux, line-of-sight velocity, and velocity dispersion for clumpy galaxies. Galaxies are ordered in increasing SFR from left to right. Also shown is the redshift of each galaxy. All galaxies are observed for 10 hours at the 20×20 mas scale. Velocity structure is evident even at the lowest SFRs and the velocity dispersion maps show internal structure of ~ 5 -6 spaxels diameter (~ 500 pc radius) for the faintest galaxy down to ~ 3 spaxels (~ 250 pc radius) for the brightest galaxy.

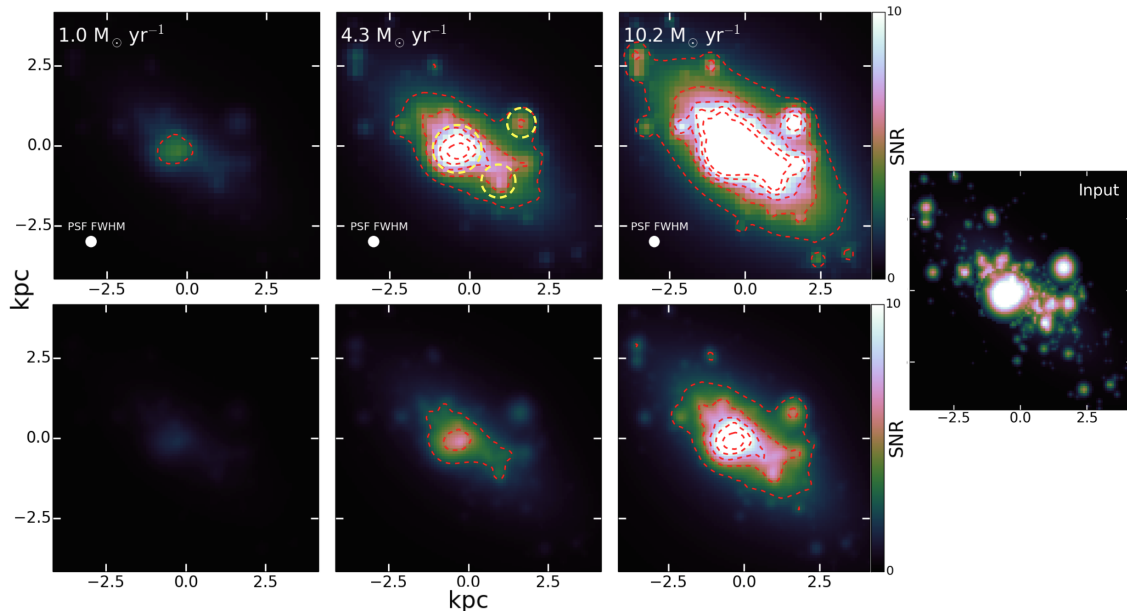


Figure 11. SNR maps of a model clumpy galaxy for varying SFRs observed at 20×20 mas (top row) and 10×10 mas (bottom row). SFR increases from left to right and is denoted in the top left of each panel. The size of the LTAO PSF is shown in the bottom left of the each map in the top row. The total exposure time is 10 hours. The three star-forming clumps detected by CLUMPFIND are highlighted with yellow dashed circles in the central panel of the top row. For comparison we also show the input morphology (10 mas sampling) in the right hand subplot. Sub-kpc sized star forming regions are detected with $SNR > 5$ for $SFR \sim 4 M_{\odot}$ at 20mas. Similar regions are detected for $SFR \sim 10 M_{\odot}$ at 10mas.

generation instruments. By deriving rotation curves we find that the E-ELT with HARMONI offers improved resolution data with a 10 fold improvement in observing efficiency compared to current telescopes, i.e. in equal observing times the E-ELT could observe 10 times as many objects. For equal observing times on the same galaxy the increased sensitivity of the E-ELT with HARMONI gives a factor of ~ 2 improvement in dynamical mass estimates.

5. HARMONI with LTAO will provide exquisite resolved spectroscopy of $z \sim 2$ –3 galaxies, allowing the detection of individual star forming complexes and measurements of their properties. We demonstrate that it will be possible to detect star forming HII regions down to at least ~ 500 pc radius in a galaxy of $\text{SFR} = 4 M_{\odot} \text{ yr}^{-1}$ in a single night. We stress that this is only a representative example and a more detailed analysis of star forming clumps will be presented in a later work.

ACKNOWLEDGMENTS

We are grateful to the anonymous referee for helpful feedback which improved this paper. The authors also thank N. Schwartz for providing AO PSFs, M. Puech for helpful feedback while testing our pipeline, and J. Liske for help using *eltpsfitt*. SZ, NT, SK, RH, MT and FC are supported by STFC-HARMONI grant ST/J002216/1. RH was also supported by STFC grant numbers ST/H002456/1 & ST/K00106X/1. AMS acknowledges an STFC Advanced Fellowship (ST/H005234/1) and the Leverhulme foundation.

REFERENCES

- Armus L. et al., 2009, PASP, 121, 559
 Astropy Collaboration et al., 2013, A&A, 558, A33
 Chabrier G., 2003, PASP, 115, 763
 Courteau S., 1997, AJ, 114, 2402
 Dorner B. et al., 2011, in Astronomical Society of the Pacific Conference Series, Vol. 442, Astronomical Data Analysis Software and Systems XX, Evans I. N., Accomazzi A., Mink D. J., Rots A. H., eds., p. 343
 Finger G., Dorn R. J., Eschbaumer S., Hall D. N. B., Mehrgan L., Meyer M., Stegmeier J., 2008, in Society of Photo-Optical Instrumentation Engineers (SPIE) Conference Series, Vol. 7021, Society of Photo-Optical Instrumentation Engineers (SPIE) Conference Series, p. 0
 Förster Schreiber N. M. et al., 2009, ApJ, 706, 1364
 Förster Schreiber N. M. et al., 2006, ApJ, 645, 1062
 Förster Schreiber N. M., Shapley A. E., Erb D. K., Genzel R., Steidel C. C., Bouché N., Cresci G., Davies R., 2011a, ApJ, 731, 65
 Förster Schreiber N. M. et al., 2011b, ApJ, 739, 45
 Genzel R. et al., 2006, Nature, 442, 786
 Glazebrook K., 2013, PASA, 30, 56
 Horne K., 1986, PASP, 98, 609
 Jarno A., Bacon R., Ferruit P., Pécontal-Rousset A., 2008, in Astronomical Society of the Pacific Conference Series, Vol. 394, Astronomical Data Analysis Software and Systems XVII, Argyle R. W., Bunclark P. S., Lewis J. R., eds., p. 701
 Jones A., Noll S., Kausch W., Szyszka C., Kimeswenger S., 2013, A&A, 560, A91
 Jones T. A., Swinbank A. M., Ellis R. S., Richard J., Stark D. P., 2010, MNRAS, 404, 1247
 Kennicutt, Jr. R. C., 1998, ApJ, 498, 541
 Law D. R., Steidel C. C., Erb D. K., Larkin J. E., Pettini M., Shapley A. E., Wright S. A., 2007, ApJ, 669, 929
 Law D. R., Steidel C. C., Erb D. K., Larkin J. E., Pettini M., Shapley A. E., Wright S. A., 2009, ApJ, 697, 2057
 Livermore R. C. et al., 2012, MNRAS, 427, 688
 Livermore R. C. et al., 2015, MNRAS, 450, 1812
 Lorente N. P. F., Glasse A. C. H., Wright G. S., Ramsay S. K., Evans C. J., 2008, in 2007 ESO Instrument Calibration Workshop, Kaufer A., Kerber F., eds., p. 295
 Madau P., Dickinson M., 2014, ARA&A, 52, 415
 Noll S., Kausch W., Barden M., Jones A. M., Szyszka C., Kimeswenger S., Vinther J., 2012, A&A, 543, A92
 Piqueras L. et al., 2010, in Society of Photo-Optical Instrumentation Engineers (SPIE) Conference Series, Vol. 7738, Society of Photo-Optical Instrumentation Engineers (SPIE) Conference Series, p. 12
 Puech M., Flores H., Lehnert M., Neichel B., Fusco T., Rosati P., Cuby J.-G., Rousset G., 2008, MNRAS, 390, 1089
 Puech M., Rosati P., Toft S., Cimatti A., Neichel B., Fusco T., 2010, MNRAS, 402, 903
 Puech M., Yang Y. B., Flores H., 2010, in Society of Photo-Optical Instrumentation Engineers (SPIE) Conference Series, Vol. 7735, Society of Photo-Optical Instrumentation Engineers (SPIE) Conference Series, p. 5
 Robertson J. G., 1986, PASP, 98, 1220
 Roe H. G., 2002, PASP, 114, 450
 Schubert G., Walterscheid R. L., 2000, in Allen's Astrophysical Quantities, Cox A. N., ed., 4th ed.; New York: AIP, p. 239
 Swinbank M., Smail I., Sobral D., Theuns T., Best P., Geach J., 2012a, ArXiv e-prints
 Swinbank M., Sobral D., Smail I., Geach J., Best P., McCarthy I., Crain R., Theuns T., 2012b, ArXiv e-prints
 Thatte N. et al., 2010, in Society of Photo-Optical Instrumentation Engineers (SPIE) Conference Series, Vol. 7735, Society of Photo-Optical Instrumentation Engineers (SPIE) Conference Series, p. 2
 Williams J. P., de Geus E. J., Blitz L., 1994, ApJ, 428, 693
 Wisnioski E. et al., 2015, ApJ, 799, 209
 Zieleniewski S., Thatte N., 2013, in Proceedings of the Third AO4ELT Conference, Esposito S., Fini L., eds., p. 43
 Zieleniewski S., Thatte N., Kendrew S., Houghton R., Tecza M., Clarke F., Fusco T., Swinbank M., 2014, in Society of Photo-Optical Instrumentation Engineers (SPIE) Conference Series, Vol. 9147, Society of Photo-Optical Instrumentation Engineers (SPIE) Conference Series, p. 93

This paper has been typeset from a \TeX / \LaTeX file prepared by the author.